Design of Broadband Low-profile Transmitarrays at Ka-band with High-Permittivity 3D-printed Materials

Yang Cai, *Student Member*, *IEEE*, Sérgio A. Matos, *Senior Member*, *IEEE*, Peng Mei, *Senior Member*, *IEEE*, João M. Felício, *Member*, *IEEE*, Carlos A. Fernandes, *Life Senior Member*, *IEEE*, Jorge Costa, *Senior Member*, *IEEE*, and Shuai Zhang, *Fellow*, *IEEE*,

***Abstract* — Transmitarrays (TAs) are a cost-effective solution for millimeter-wave antenna applications. The widespread use of fully dielectric TAs (DTAs) emerges from the manufacturing simplicity brought by 3D printing. Previously reported DTAs employ readily available low-permittivity materials (ε_r < 3). However, this implementation implies thicker lenses (exceeding one free space wavelength, > λ_0), affecting the DTA performance compared with thinner TA based on printed-circuit-board (PCB) technology. This work shows that, when properly crafted, 3D-printed high-permittivity dielectric (HPD) materials can solve this problem. The design challenge is to circumvent the free-space mismatch and narrowband responses usually associated with HPD materials. A commercially available HPD material compatible with 3D printing is used as an example to demonstrate the feasibility of this type of DTA. This study includes the in-house material characterization for the designed frequency (ε_r = 13.1 at 30 GHz). A HPD TA is benchmarked against a conventional PCB-based TA for evaluating the impact of HPD materials for the design of this type of TA. A HPD TA with a diameter of 14 λ_0 (λ_0 is the wavelength at 30 GHz in free space) and a height of 0.4 λ_0 (excluding the feed horn) is fabricated with the low-cost 3D printing method of fuse deposition modeling (FDM). When illuminated by a standard horn, the HPD TA antenna provides a 27.4 dBi gain, elevation scanning up to 45 degrees (through the horizontal displacement of the feed horn) with a scan loss of 2 dB and a 1-dB gain bandwidth of 16.3%.**

***Index Terms*—Transmitarray antennas, dielectric antennas, high-permittivity dielectric material, three-dimensional (3-D) printing techniques.**

I. Introduction

Transmitarray (TA) antennas, generally consisting of a TA and a feed source, play a significant role in millimeter-wave communications [1]-[3], owing to their simple structure, ease of fabrication, low cost, and high design flexibility. A TA acts as a lens that shapes the phase of the incoming electromagnetic wave radiating from a feed source. Its operating principle is based on diffractions rather than refractions, distinguishing it from conventional dielectric lenses such as the zoned lens [4]. In this context, the TA shares a similar operational principle with the Fresnel lens [5], [6]. However, instead of using concentric rings, TAs are composed of engineered unit cells (UCs) – commonly referred to as a metasurface. Far greater flexibility is achieved with TA, as a wider range of geometries and material combinations can be explored to achieve the desired phase shift and transmission characteristics.

There are two main approaches for implementing the UCs that comprise the TA. One approach employs printed-circuit-board (PCB) - based UCs, consisting of a multilayer stack with patterned metal layers, referred to throughout this paper as PCB TA [7]-[9]. A second approach consists of using only dielectric materials for the UC design, offering the advantage of compatibility with low-cost 3D printing fabrication techniques [10]-[18]. Compared to PCB-based UCs, fully dielectric UCs provide greater design flexibility enabling a wider range of geometries, including conformal TA antenna [19], with lower fabrication time and cost. Moreover, they typically provide a wider bandwidth. On the other hand, achieving the desired phase range requires significantly thicker UCs compared to PCB implementations. For instance, the profile of the UC usually exceeds one wavelength in free space when the dielectric constant is less than 5.0. In [10], the authors employed a dielectric material with a relative permittivity of 3.4 to implement a TA, resulting in a total profile of 3.0 λ. The high profile of low-permittivity-based dielectric TAs can be a major drawback in certain applications. For instance, such 3D-printed TAs are often integrated into leaky-wave feeding systems (as shown in [20]), where component spacing can be as small as λ/10. In these scenarios, it becomes essential to minimize both the distance between metasurfaces and the overall thickness of the TA to substantially reduce the antenna profile – a key requirement for compact antenna terminal design.

In this paper, we explore the potential of using high-permittivity dielectric (HPD) materials to achieve a unique combination of low profile, high gain, and wide bandwidth,

This work was supported in part by China Scholarship Council (CSC), in part by innovationsfonden project of DRONE, in part by DFF Project 1, in part by FCT/MECI through national funds and co-funded EU funds under UID/50008: Instituto de Telecomunicações. (*Corresponding author: Peng Mei.*)

Y. Cai, P. Mei and S. Zhang are with the Antennas, Propagation and Millimeter-Wave Systems (APMS) Section, Department of Electronic Systems, Aalborg University, 9220 Aalborg, Denmark (e-mail: yangc@es.aau.dk, mei@es.aau.dk, sz@es.aau.dk).

Sérgio A. Matos, João M. Felício, Carlos A. Fernandes, and Jorge Costa are with the Instituto de Telecomunicações, Instituto Superior Técnico, Universidade de Lisboa, 1049-001 Lisbon, Portugal, Sérgio A. Matos and Jorge Costa are also with the Departamento de Ciências e Tecnologias da Informação, Instituto Universitário de Lisboa, 2649-026 Lisbon, Portugal. João M. Felício is also with the Centro de Investigação Naval, Instituto Universitário Militar, 2810-001 Almada, Portugal. (e-mail: Sergio.Matos@iscte-iul.pt, joao.felicio@lx.it.pt, carlos.fernander@lx.it.pt, jorge.costa@iscte-iul.pt).

which is unattainable with low-permittivity dielectric materials. To the authors' best knowledge, there is currently no implementation of a TA antenna using a monolithic block of HPD (i.e., $\varepsilon_r > 12$). In [15], the authors presented a 3D-printed transformed hyperbolic flat lens operating in the 30 GHz band. The lens was fabricated using a single HPD material — acrylonitrile butadiene styrene (ABS) 1200 — with a dielectric constant of 12.0. Based on transformation optics principles, the required permittivity distribution across the lens was achieved by varying the infill percentage during the printing process. Nevertheless, the total profile reached 12 mm, corresponding to 1.2 λ at 30 GHz in free space. In [16], the authors designed a flat lens by combining different types of ABS materials with dielectric constants of 3, 4.2, 5.4, 7.8, and 12 to achieve the desired refractive index for beam collimation. However, this approach significantly increases the complexity of fabrication and assembly. In [21], a TA was implemented using a combination of two materials ($\varepsilon_r = 6$ and $\varepsilon_r = 3$), resulting in an overall thickness of 0.75 λ—approximately twice the thickness of our design. This implementation exhibited limited aperture efficiency due to fabrication constraints and the limited availability of suitable HPD materials. These examples highlight the significant challenges associated with realizing high-permittivity 3D-printed TAs, thereby underscoring the novelty of the approach presented in this work.

From the perspective of transmission theory, the profile can be effectively reduced by employing HPD materials. However, the design of TAs using HPD materials differs significantly from those based on low-permittivity dielectric materials. This difference arises from more complex wave-material interactions caused by increased free-space mismatch, stronger diffraction effects, and total internal reflections. Only under specific conditions can the design simplicity of low-permittivity solutions be retained while achieving comparable bandwidth and transmissivity — with the added benefit of significantly thinner metasurfaces. More specifically, an air cavity on the top and bottom surfaces of the HPD UC is optimized to reduce reflections, effectively acting as a matching layer. Moreover, the periodicity of the HPD UC is reduced to suppress guided modes within the frequency range of interest, which are enabled by total internal reflections — an effect that can significantly impact the TA bandwidth.

A commercially available material, ABS1500, with a dielectric constant of 13.1 and a loss tangent of 0.046 characterized at 30 GHz, has been utilized to implement a HPD TA antenna. The total profile of the HPD TA (excluding the feed source) is only 0.4 λ, enabling a 2-bit transmission phase quantization. The developed HPD TA antenna prototype presents a 1-dB gain bandwidth of 16% and a peak aperture efficiency of 28%, in good agreement with simulations. Additionally, simulation results are compared with an equivalent PCB-based TA antenna to illustrate the aforementioned trade-offs between the two technologies.

The paper is organized as follows. Section II presents the design principles for all-dielectric UCs with high-permittivity materials. Two TA antennas with a 2-bit phase quantization using HPD UCs and conventional PCB-based UCs are designed and simulated in Section III. Measurements of the HPD material and the prototype, as well as comparisons with the literature, are detailed in Section IV. Section V concludes this paper.

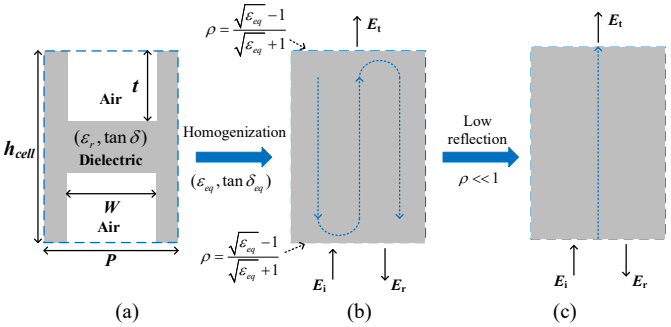

Fig. 1. (a). Monoblock dielectric UC. (b) Slab model of the UC, according to the homogenization model. (c). Single ray model of the UC, traveling along a homogenized dielectric.

II. Unit Cell Design and Analysis

A. Modeling of dielectric UCs

All-dielectric UCs are typically analyzed using a homogenized model. In this approach, as depicted in Fig. 1(a), a mixture of air and dielectric material – with relative permittivity ε_r and loss tangent $\tan\delta$ – is approximated as an equivalent homogeneous dielectric medium. This equivalent medium is characterized by an effective permittivity ε_{eq} and an effective loss tangent $\tan\delta_{eq}$. These effective parameters are determined by averaging the permittivity values of the constituent materials, weighted according to their respective filling factors [22]

$$\varepsilon_{eq} = 1 + (\varepsilon_r - 1) V_{diel} / V_{cell} \tag{1}$$

$$\tan\delta_{eq} = \frac{V_{diel}}{V_{cell}} \frac{\varepsilon_r}{\varepsilon_{eq}} \tan\delta \tag{2}$$

where V_{diel} is the volume of the dielectric, and V_{cell} is the total volume of the UC (i.e., dielectric + air). The Floquet analysis (i.e., the UC under periodic boundary conditions) of the homogenized UC reduces to the canonical problem of a dielectric slab, as illustrated in Fig. 1(b). The corresponding scattering response of the homogenized UC is given by the canonical transmission coefficient of a dielectric slab [23]

$$S_{21}^{slab} = \frac{(1-\rho^2)e^{-jk_0 n h_{cell}}}{1-\rho^2 e^{-2jk_0 n h_{cell}}} \tag{3}$$

where k_0 is the prapagtion constant, h_{cell} is the UC height, $\rho = \frac{n-1}{n+1}$ is the reflection coefficient at the air-dielectric interface and n is the complex refractive index of the effective material. For $\tan\delta << 1$, the refractive index can be approximated as

$$n = \sqrt{\varepsilon_{eq}(1 - j\tan\delta_{eq})} \approx \sqrt{\varepsilon_{eq}}\left(1 - \frac{j}{2}\tan\delta_{eq}\right) \tag{4}$$

For low reflections at the air–dielectric interface (i.e., $\rho << 1$), the model can be further simplified using a single-ray approximation, as illustrated in Fig. 1(c). Under this condition, Eq. (3) can also be simplified, and the amplitude and phase response of the UC can be directly obtained by substituting Eq. (4) into Eq. (3):

$$|S_{21}| = e^{-\frac{\pi}{\lambda}\sqrt{\varepsilon_{eq}}\tan\delta_{eq}h_{cell}} \tag{5.a}$$

$$\phi_{cell} = \arg(S_{21}) = \frac{2\pi}{\lambda}\sqrt{\varepsilon_{eq}}h_{cell} \tag{5.b}$$

However, it is noted that this simplified model should be applied with caution when dealing with HPD materials, as discussed in the following section.

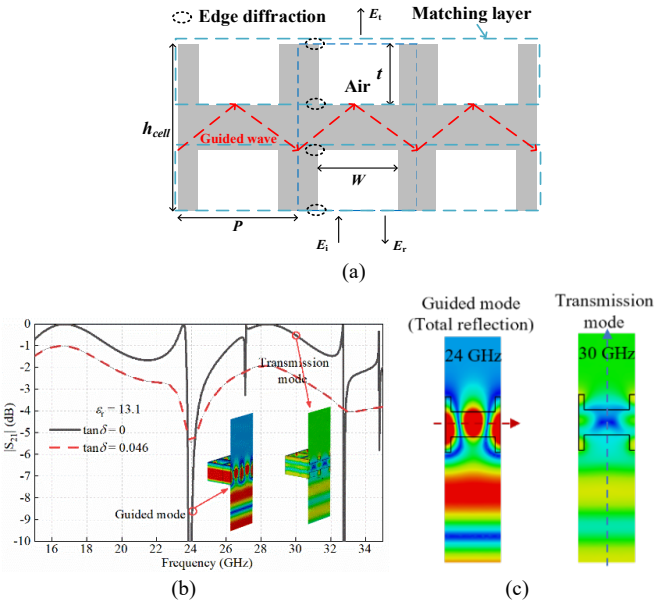

Fig. 2. (a). Schematic illustration of guided and transmission modes within the UC. (b). The simulated transmission coefficient of the UC for both lossless and lossy cases, assuming $\varepsilon_r = 13.1$, $P = 4.0$ mm, $h_{cell} = 4$ mm, $W = 3.2$ mm, $t = 1.1$ mm. (c) Electric field distributions at 24 GHz and 30 GHz, corresponding to guided and transmission modes, respectively.

B. Characterization of the high-permittivity dielectric material at a broad frequency band

The material that will be employed to demonstrate the potential of HPD UC is PREPERM ABS1500 [24], which, to the best of our knowledge, offers the highest permittivity among materials compatible with low-cost FDM printing. According to the datasheet, its electromagnetic properties are $\varepsilon_r = 15$ and $\tan\delta = 0.018$ @ 2GHz. Since these values are specified only at low frequencies, we characterize the material at 30 GHz to validate its suitability for the proposed design. To facilitate the characterization, several test samples (solid cubes and plates) of ABS 1500 are printed using the described settings. Given that permittivity measurements are highly sensitive to dimensional uncertainties, the permittivity and loss tangent of the samples are characterized using three methods: SPEAG DAK-TL2 dielectric assessment kit [25], free-space method using a Gaussian beam, and a waveguide method [26]. The measured results from all three methods are consistent. The measured relative permittivity and loss tangent with the SPEAG DAK-TL2 toolkit are plotted in Fig. 3. It is worth noting that the pressure applied to the sample affects the measured permittivity due to tiny air gaps in the sample, which are inevitable with FDM printing technology. Lower applied pressure retains more air in the sample, leading to lower permittivity as illustrated in Fig. 3, which may be alleviated with stereolithography (SLA) or PolyJet printing technologies.

It is observed that significant differences relative to the datasheet values were measured at 30 GHz: $\varepsilon_r = 13.1 \pm 1.0$ (depending on the applied pressure, see Fig. 3) and $\tan\delta = 0.045$. The uncertainty in the permittivity corresponds, in the worst case, to a phase variation of ± 20°, according to Eq. (5), which has a limited impact on a 2-bit TA. On the other hand, the increase in loss tangent relative to the initially expected value is estimated to cause a gain drop of the corresponding TA antenna at least 1.0 dB.

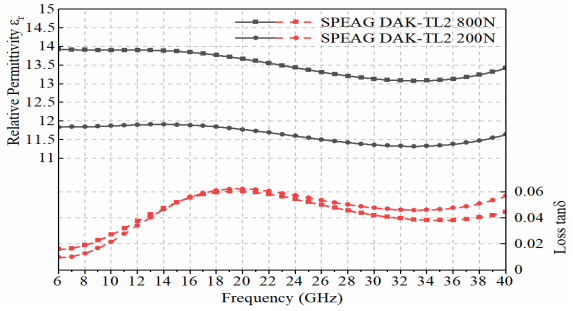

Fig. 3. Measured dielectric permittivity and loss tangent of ABS 1500.

A. Design of high permittivity dielectric UCs

As previously mentioned, the design of HPD UC presents additional challenges, including: (i). mitigating the inherent and severe free-space impedance mismatch over a wide bandwidth, and (ii). avoiding the excitation of guided modes caused by total internal reflections, which appear as resonances in the transmission response of the UC.

The first issue can be addressed by engineering a local field distribution that acts as a matching layer. As shown in Fig. 2(a), two air cuboids embedded at the top and bottom surfaces of the UC are optimized – simply tuning the parameters t and W – to enhance overall transmission across a broad frequency range. Without these inclusions, the combined effects of free-space mismatch and dielectric losses would degrade UC performance.

On the other hand, the inclusion of the matching layer can excite transverse guided modes, enabled by total internal reflections within the UC, as represented in Fig. 2(a). An illustrative example is provided for a UC with $\varepsilon_r = 13.1$, $P = 4.0$ mm, $h_{cell} = 4$ mm, $W = 3.2$ mm, and $t = 1.1$ mm. The corresponding transmission is evaluated over the 15–35 GHz frequency range. The UCs are simulated in CST Microwave Studio, using the frequency domain solver under periodic boundary conditions. Field monitors are placed at relevant frequencies to capture the various interactions between a normal incidence plane wave and the UC structure. As shown

in Fig. 2(b), transmission nulls appear around 24 GHz and 32.5 GHz, attributed to the excitations of guided modes. In Fig. 2(c), the electric field distribution at 24 GHz shows the extreme case where the UC converts an incident plane wave into a transverse guided mode. When the loss tangent of the UC is considered, corresponding to the red curve in Fig. 2(b), the influence of the guided modes in the UC transmission coefficient becomes less pronounced, but they still introduce noticeable loss. In the frequency range between these nulls, good transmission performance is observed, as confirmed by the field distribution at 30 GHz represented in Fig. 2 (c).

The interaction between the incident plane wave and the excitation of guided modes is complex and typically requires detailed analytical treatment involving edge diffraction and mode matching. Rather than pursuing this rigorous approach, we adopt the pragmatic strategy of identifying trends during the UC optimization process. Specifically, we found that reducing the UC periodicity P, while keeping the air insertion dimensions fixed, can effectively suppress guided mode excitations within the frequency range of interest. In Fig. 4, we show for the selected periodicity of P = 2 mm (λ/5 @ 30GHz) that the UC transmissivity is no longer significantly affected by guided-mode resonances. It is worth noting that, in many designs, the UC periodicity is simply chosen a priori to be approximately λ/2, which is sufficient to prevent grating lobes.

TABLE I: DIMENSIONS OF THE HP UCS AND EQUIVALENT DESCRIPTION

UC	$P\ (mm)$	$W\ (mm)$	$t\ mm)$	$hcell(mm)$	ϵ_{eq}	$\tan\delta_{eq}$
0	Air			4	1	0
1	2	1.6	1.1	2.2	3.4	0.034
2			1.9	4	5.7	0.040
3			1.1	4	8.8	0.043

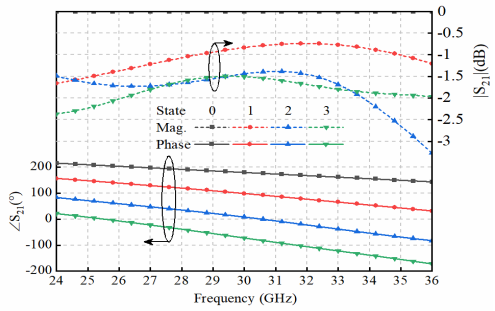

Fig. 4. The transmission phase and magnitude of the four-UCs under normal incidence. (ε_r = 13.1, tan δ = 0.046, P = 2.0 mm)

The UCs should be designed to provide a specific phase range, $\Delta\phi_{max}$, to construct a TA, using a given discretization step. Taking air as the reference case (ε_{eq} = 1), it follows from Eq. (5) that the minimal required height is given by

$$h_{cell} > \frac{\lambda}{\sqrt{\varepsilon_r}-1}\frac{\Delta\phi_{\max}}{2\pi} \tag{6}$$

which corresponds to a UC composed of a single, homogeneous dielectric block (ε_{eq} = ε_r). In principle, the UC can achieve continuous phase tuning across the full 360° coverage by appropriately adjusting its geometric parameters. However, for HPD materials, this tuning becomes significantly more complex compared to low-permittivity dielectric cases. Moreover, the achievable phase coverage is constrained by the resolution and accuracy of the 3D printer used in this study. Based on extensive simulations and fabrication trials, we determined that the proposed UC can reliably achieve approximately phase coverage of 300° at a profile of 4 mm using our available 3D printer, which is slightly higher than the minimum height to achieve the same phase coverage calculated with Eq. (5). Beyond this range, the required fine structural variations surpass the printer's resolution, often resulting in fabrication failures. Nevertheless, it still results in a significantly thinner profile compared with low-permittivity dielectric materials (a typical thickness above λ). To ensure robust manufacturability and consistent performance, we therefore adopted a 2-bit phase quantization.

TABLE II: PHASE AND AMPLITUDE OF THE HP UC RESPONSES AT 30 GHZ

	Full-wave		Ray Model		Slab
UC	$\Delta\phi$ (°)	$\lvert S_{21}\rvert$(dB)	$\Delta\phi$ (°)	$\lvert S_{21}^{ray}\rvert$ (dB)	$\lvert S_{21}^{slab}\rvert$ (dB)
0	0	0	0	0	0
1	81	-0.8	121	-0.7	-2.1
2	172	-1.4	201	-1.1	-1.6
3	252	-1.5	284	-1.4	-5.0

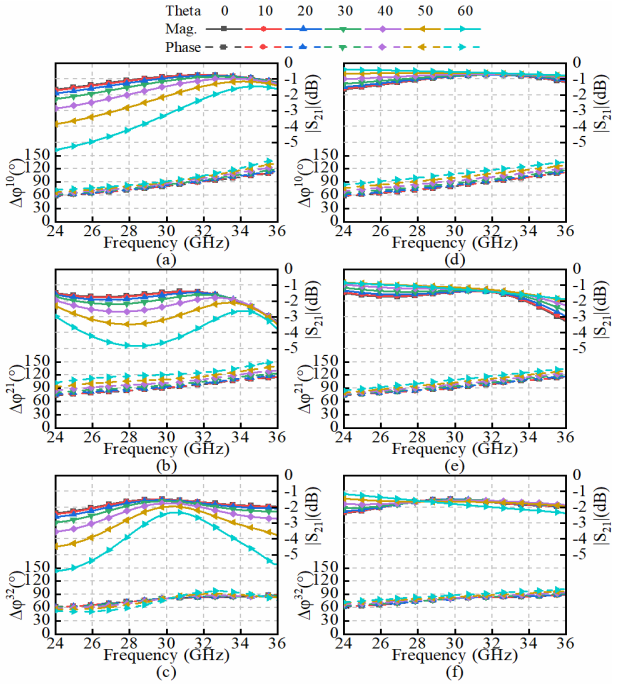

Fig. 5. The transmission magnitude and relative phase of the UCs under (a)-(c) TE and (d)-(f) TM oblique incidence up to 60°, for states 1 to 3, respectively.

The dimensions of the UCs are optimized and obtained to offer the desired 2-bit phase quantization, as listed in Tab. I. Furthermore, the equivalent relative permittivity and loss tangent of the four UCs are calculated with Eqs. (1) and (2), as also presented in Tab. I. The corresponding amplitude and phase responses of the four UCs are firstly simulated under normal incidence and plotted in Fig. 4. As expected, these four

UCs exhibit wideband performance, achieving transmission loss below 3 dB from 24 to 36 GHz, while consistently maintaining 2-bit phase quantization. In Tab. II, the phase and amplitude responses of the UCs at the frequency of interest (i.e., 30 GHz) are compared with the Ray (Eqs. (4) and (6)) and Slab models (Eq. (3)). In this case, where the UC operates with a single transmission mode as shown in Fig. 2(c), we confirm that the phase variations are reasonably well described by the single-ray model, with discrepancies remaining below 40°. At the frequency of interest, the amplitude response approaches the upper limit predicted by the single-ray approximation. Conversely, the slab model provides a lower bound for the expected UC performance. In the proposed design, UC's amplitude response is primarily limited by material losses. Nevertheless, we demonstrate that even under high-loss conditions, it is still feasible to realize competitive TA. Most importantly, the design methodology presented is broadly applicable and can be extended to future accessible 3D-printable, low-loss, high-permittivity dielectric materials.

The transmission responses of the four UCs under different oblique incidences of TE and TM polarizations are also studied. The phase difference between states $\Delta\phi^{mn} = \arg(S_{21}^{n}) - \arg(S_{21}^{m})$ is plotted here for a better comparison since the UC state 0 is pure air. As shown in Fig. 5, robust phase responses up to 40° of oblique incidence for both TE and TM polarizations are observed. The maximum phase difference deviations in all states remain within 30° at 30 GHz. This angular stability of the UC is primarily attributed to both smaller periodicity and thinner profile enabled by the use of HPD materials.

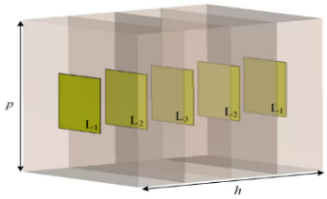

Fig. 6. Geometry of the PCB-based UC. (p = 2.5 mm)

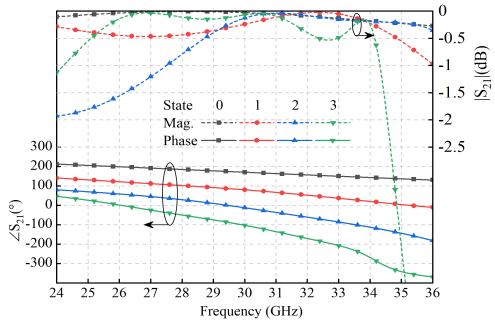

Fig. 7. The transmission phase and magnitude of the selected 2-bit PCB UCs.

B. Multi-layered PCB UC design

A comparison between the fully dielectric UC and a PCB-based UC is carried out to highlight the advantages of each technology. For this purpose, we consider a subset of UCs previously reported in [27], which have been implemented in a wide range of applications. The complete set includes 63 UCs that provide a discretization step of approximately 6°, covering a phase range from 0° to 333°, with a transmission loss better than –0.4 dB across the 29–30 GHz bandwidth. This design consists of four substrate layers and five layers of square patches, as illustrated in Fig. 6. The periodicity of the UC is 2.5 mm, and the total thickness is 3.2 mm (0.32λ at 30 GHz), making it comparable in profile to the proposed HPD UC. For a fair comparison, we selected the best-performing UCs from this set that support 2-bit phase quantization (as in the developed prototype) while maintaining the widest possible bandwidth. As such, we consider this PCB design representative of the performance achievable with this technology. The dimensions of the selected PCB-based UCs are listed in Table III, and their corresponding transmission magnitude and phase responses are shown in Fig. 7.

TABLE III: DIMENSIONS OF THE PCB-BASED UCS

	Parameter (unit: mm)	State 0	1	2	3
PCB UC	L_1	0.9	1.71	1.88	2.13
	L_2	0.9	1.63	2.21	2.31
	L_3	0.9	1.9	2.13	2.21

III. IMPLEMENTATION OF THE TRANSMITARRAYS

In this section, we compare two implementations of the same TA design: one based on HPD UCs and the other on PCB UCs. The baseline configuration is illustrated in Fig. 8. The TAs are designed to generate a tilted collimated beam at an angle of α_0 on the *xoz*-plane. The required phase compensation for the incident spherical wavefront is given by:

$$\psi_{mn} = k_0\sqrt{x_{mn}^2 + y_{mn}^2 + F^2} - k_0 x_{mn}\sin\alpha_0 \tag{7}$$

where k_0 is the wave number in free space; (x_{mn}, y_{mn}) is the position of the *mn*-th UC on the *xoy*-plane. Ideally, the UC phase correction would continuously follow the wrapped phase values of Eq. (7) calculated at (x_{mn}, y_{mn}). In Fig. 9 (a), the continuous phase profile is represented for the wrapped interval of -180º to 180º, according to

$$\Delta\phi = \frac{180}{\pi}\left[\mathrm{mod}\left(\psi_{m,n} + \pi, 2\pi\right) - \pi\right] \tag{8}$$

As mentioned earlier, a 2-bit phase quantization was chosen for implementing the HPD and PCB-based UCs, which implies selecting the UC state according to

$$State = \begin{cases} 0, & -180^\circ < \Delta\phi < -90^\circ \\ 1, & -90^\circ < \Delta\phi < 0^\circ \\ 2, & 0^\circ < \Delta\phi < 90^\circ \\ 3, & 90^\circ < \Delta\phi < 180^\circ \end{cases} \tag{9}$$

The corresponding UC distributions for the two TAs are shown in Figs. 9 (b) and (c). It is noted that, due to the slight

difference in periodicity between the HPD and the PCB-based UCs, the resulting phase distributions in Figs. 9 (b) and (c) differ accordingly. The geometries of the two TAs are finally established and shown in Fig. 10.

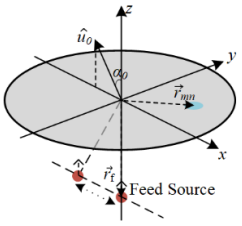

Fig. 8. A general configuration of a TA antenna.

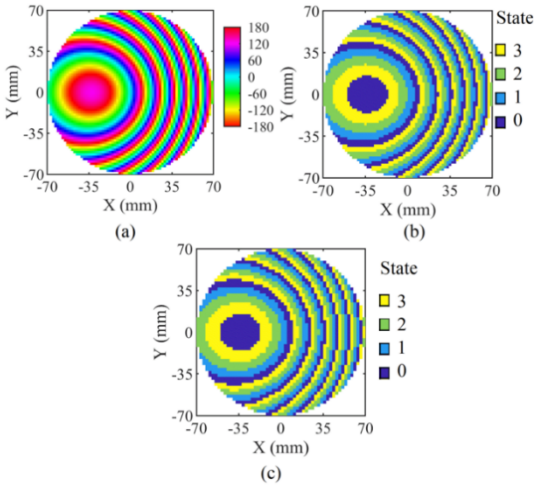

Fig. 9. (a) Continuous phase compensation of the TA. The corresponding discrete states distribution of the (b) HPD and (c) PCB UCs.

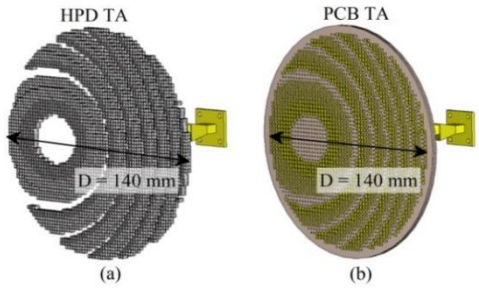

Fig. 10. Geometry of the (a) HPD TA, and (b) PCB TA.

A linearly polarized standard 12 dBi horn antenna is used as the primary feed source for illuminating the two TAs. The horn antenna is aligned along the *z*-axis and positioned at a focal distance of F = 70 mm, corresponding to an F/D ratio of 0.5. This configuration corresponds to an edge taper of -12.7 dB at 30 GHz, providing a good compromise between aperture efficiency and overall antenna profile. The implemented TA antennas are simulated in CST Microwave Studio using the built-in FDTD solver. The simulated radiation patterns are shown in Fig. 11. Both TA antennas exhibit similar radiation patterns; however, the realized gain of the HPD TA antenna is 1.0 dB lower due to the higher material losses associated with the HPD material. As a result, the radiation efficiency at 30 GHz is 82.2% for the HPD TA antenna, compared to 97.8% for the PCB-based TA antenna. Nevertheless, the maximum aperture efficiency of the HPD TA antenna reaches 32.7% at 31 GHz, which is already a competitive value compared to other designs (as shown later in Table IV).

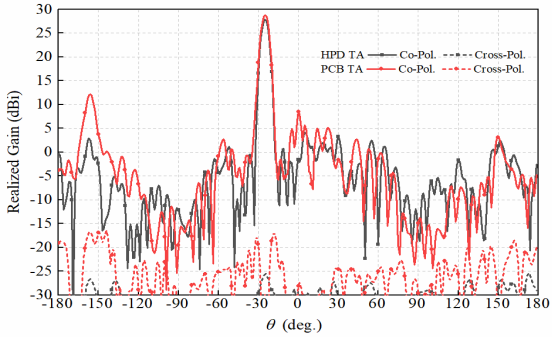

Fig. 11. Simulated radiation pattern of the HPD TA and PCB TA at 30 GHz.

IV. Experimental Results

A. Guidelines for 3D printing high-permittivity dielectric materials

To validate the full-wave simulations, the HPD TA is fabricated using our available 3D printer (Raised 3D pro2), employing deposition modeling (FDM) with the filament of acrylonitrile butadiene styrene 1500 (ABS 1500). There are some important issues to consider for HPD material printing: 1). smaller tensile stress and tensile strain using a test method with the standard of ISO 572-2, which are 14 MPa and 5% for ABS 1500, respectively; 2). inconsistent extrusion due to moisture absorbing of the HPD material from ambient air. Therefore, it is recommended to heat the filament in an oven at 80°C for 4 - 5 hours to dehydrate it prior to printing. In addition, specific parameters of the 3D printer used must be carefully configured to permit successful printing, and are then listed as follows: the temperatures of the heat bed and the extruder are 100°C and 260°C, respectively, the layer height is 0.15 mm, the infill density is 100% with the infill pattern type of rectilinear, the flow rate is 115%, the printing speed is limited to 30 mm/s since high printing speed usually causes more inconsistent extrusion. It is worth noting that these settings may vary depending on the specific 3D printer used and filament properties. As a result, we recommend printing small samples to fine-tune the settings before printing the whole prototype.

B. Measurement of the prototype of a HPD TA antenna

To facilitate the measurement, a 3D-printed ring frame and fixture are designed to precisely assemble the HPD TA and the feed horn, as shown in Figs. 12(a) and (b), which are printed using PLA material with a dielectric constant of 2.2. The prototype is measured in the anechoic chamber with the measurement setup illustrated in Fig. 12 (c). The prototype, referred to as the AUT (antenna under test), is mounted on a pole and rotates in the azimuth plane and the receiving antenna rotates along an arc centered at the AUT. To enable beam

steering of the HPD TA antenna, the feed horn is horizontally displaced along the *x*-axis from -31 mm to 25 mm, resulting in the scanning beams from -5° to -45°. The simulated and measured radiation patterns of the HPD TA antenna at 30 GHz are plotted in Fig. 13. Despite a small discrepancy in the realized gain, the beam directions and sidelobe levels demonstrate excellent agreements. The measured sidelobe levels of all scanning beams are below -13 dB. Furthermore, the realized gain of the HPD TA antenna with frequency is also measured and presented in Fig. 14, where the simulated counterpart is also plotted for comparison. It is shown that the peak directivity of the HPD TA antenna is nearly identical to that of the PCB-based TA antenna, confirming that both TA antennas exhibit similar performance, aside from the impact of material losses. It is observed that the HPD TA antenna exhibits a wider 1-dB bandwidth (15.6%) compared to that (10%) of the PCB-based TA antenna, which demonstrates one of the advantages of the proposed HPD TA antenna experimentally.

The small discrepancy between the measured and simulated results can be partially attributed to the printing tolerances of the 3D printer used. Since small air cavities are drilled in the top and bottom surfaces of the HPD UC to form the matching layers, the bridge feature of the 3D printer is utilized during the printing process, which allows small hovering structures. However, the relatively low printing speed results in a rough and uneven hovering surface, which degrades the effectiveness of the matching layer and contributes to increased losses. Additionally, the uncertainty of the measured loss tangent of the HPD material may also contribute to the observed differences.

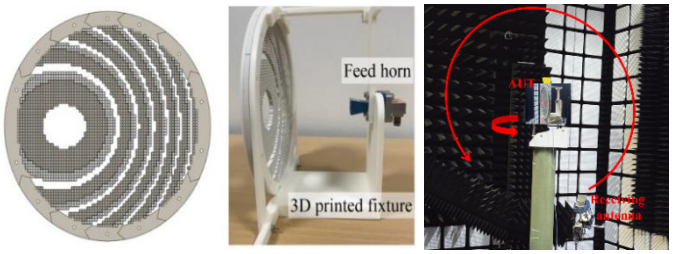

(a) (b) (c)

Fig. 12. Prototype and measurement of the HPD TA antenna. (a). Front view of the HPD TA. (b). Side view of the prototype with the 3D printed fixture and feed horn. (c). Measurement setup.

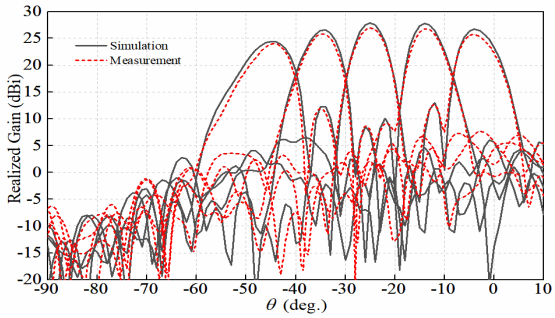

Fig. 13. Simulated and measured scanning beams with different displacements of feed horn, at 30 GHz.

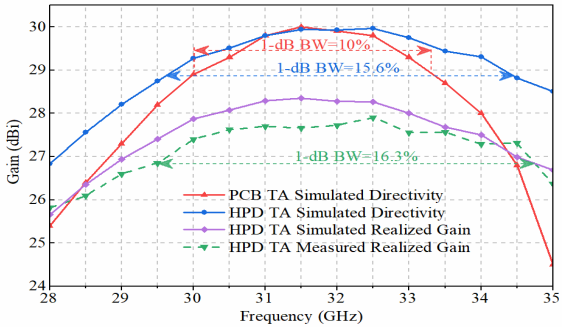

Fig. 14. Realized gain of the simulated and measured results.

The performance of the proposed HPD TA antenna is compared with dielectric-based TA antennas reported in the literature, as summarized in Table IV. The comparison focuses on printing technologies, materials, TA dimensions, gain, *F/D* ratio, aperture efficiency, and 1-dB gain bandwidth. It is observed that the proposed TA antenna, based on a HPD material, offers an ultra-low profile, comparable 1-dB gain bandwidth, and high gain. The lower aperture efficiency observed, relative to some reported designs, can be attributed to several factors: dielectric losses in the HPD material (~1 dB), phase quantization errors due to 2-bit discretization (~0.6 dB) [28], and an effective aperture reduction caused by a 25º beam offset (~0.43 dB).

TABLE IV: COMPARISON OF DIFFERENT TRANSMITARRAYS

Ref.	Freq. (GHz)	Technology	Type (Material)	Transmission phase coverage	Relative permittivity ε_r & (loss tanδ)	Overall thickness (λ_0)	F/D	Max gain (dBi)	Aperture efficiency (%)	1-dB Gain BW (%)
[10]	30	3D-printing (SLA)	Dielectric (Resin)	Continuous (2π)	3.4 (N.A.)	3	1.4	25.1	40	13.3
[11]	30	3D-printing (PolyJet)	Dielectric (RGD835)	Continuous (2π)	2.77 (0.02)	3.3	1	30.7	38	21.5
[17]	60	3D-printing (PolyJet)	Dielectric (Not mentioned)	Continuous (2π)	2.9 (0.01)	2	0.42	23.5	20	17
[29]	94	PCB drilling	Multi-layered Laminates (RO5880/RO6010)	Continuous (2π)	2.2/10.2 (0.0009/ 0.002)	1.31	0.77	30.0	25	15.9
[21]	15	3D-printing (MJF)	Dielectric (PA12)	Continuous (2π)	6 (N.A.)	0.75	0.63	23.0	11	29
HPD TA	**30**	**3D-printing (FDM)**	**Dielectric (ABS 1500)**	**Discrete (2-bit)**	**13.1 (0.046)**	**0.4**	**0.5**	**27.4**	**28**	**16.3**

V. Conclusion

This work has explored the potential of HPD materials for implementing TA antennas, addressing both benefits and challenges. Compared to the designs using low-permittivity dielectric materials, HPD-based UCs enable a significantly reduced TA profile while preserving the manufacturing benefits of 3D-printed TAs – which can enable using this technology for a wider range of applications. To address the specific challenges of working with HPD materials, a more carefully designed procedure was developed. The proposed HPD TA includes a matching layer to minimize reflections at the air–material interface and employs reduced periodicity to suppress undesired resonances within the frequency range of interest.

A prototype operating at 30 GHz demonstrates a compact profile of 0.4λ₀, an aperture efficiency of 28%, and a 1-dB gain bandwidth of 16.3%, highlighting a strong balance between size and performance. These results position the proposed HPD-based TA antenna as a competitive alternative to conventional PCB-based solutions for high-frequency applications. Future work will focus on developing HPD materials with higher permittivity and lower loss tangents to further enhance antenna performance.

References

[1]. X. Wang, Y. Cheng, and Y. Dong, "Millimeter-wave high-efficiency double-layer transmitarray antenna using miniaturized dual-polarized elements," *IEEE Trans. Antennas Propag.*, vol. 70, no. 9, pp. 8637–8642, Sep. 2022.

[2]. H. Hasani, J. S. Silva, S. Capdevila, M. Garcia-Vigueras, and J. R. Mosig, "Dual-band circularly polarized transmitarray antenna for satellite communications at (20, 30) GHz," *IEEE Trans. Antennas Propag.*, vol. 67, no. 8, pp. 5325–5333, Aug. 2019.

[3]. L.-Z. Song, T. Zhang, J.-X. Lai, Y. Yang, and J. Du, "A 180-GHz to 220-GHz wideband transmitarray with wide-angle beam steering for intersatellite communications," *IEEE Trans. Antennas Propag.*, vol. 72, no. 1, pp. 950–955, Jan. 2024.

[4]. C. A. Fernandes, *et al*., "Dielectric lens antennas," in *Handbook of Antenna Technologies*, Springer Singapore, 2016, pp. 1001–1064.

[5]. A. Jouade, M. Himdi, and O. Lafond, "Fresnel lens at millimeter-wave: enhancement of efficiency and radiation frequency bandwidth," *IEEE Trans. Antennas Propag.*, vol. 65, no. 11, pp. 5776–5786, Nov. 2017.

[6]. A. Madannejad, M. Gohari, U. Shah, and J. Oberhammer, "High-gain circularly polarized 500 – 750 GHz lens antenna enabled by silicon micromachining," *IEEE Trans. Antennas Propag.*, vol. 72, no. 5, pp. 4077–4085, May. 2024.

[7]. S. L. Liu, X. Q. Lin, Z. Q. Yang, Y. J. Chen, and J. W. Yu, "W-band low-profile transmitarray antenna using different types of FSS units," *IEEE Trans. Antennas Propag.*, vol. 66, no. 9, pp. 4613–4619, Sep. 2018.

[8]. P. Mei, G. F. Pedersen, and S. Zhang, "A broadband and FSS-based transmitarray antenna for 5G millimeter-wave applications," *IEEE Antennas Wirel. Propag. Lett.*, vol. 20, no. 1, pp. 103–107, Jan. 2021.

[9]. P. Naseri, S. A. Matos, J. R. Costa, C. A. Fernandes, and N. J. G. Fonseca, "Dual-band dual-linear-to-circular polarization converter in transmission mode application to K/Ka-band satellite communications," *IEEE Trans. Antennas Propag.*, vol. 66, no. 12, pp. 7128–7137, Dec. 2018.

[10]. F. Wei, J.-W. Hao, L. Xu, and X. Shi, "A circularly polarized 3-D printed dielectric transmitarray antenna at millimeter-wave band," *IEEE Antennas Wirel. Propag. Lett.*, vol. 20, no. 7, pp. 1264–1268, Jul. 2021.

[11]. A. Massaccesi *et al*., "3D-printable dielectric transmitarray with enhanced bandwidth at millimeter-waves," *IEEE Access*, vol. 6, pp. 46407–46418, 2018.

[12]. B. Li, *et al*., "A 3-D-printed wideband circularly polarized dielectric reflectarray of cross-shaped element," *IEEE Antennas Wirel. Propag. Lett.*, vol. 19, no. 10, pp. 1734–1738, Oct. 2020.

[13]. Y. Lei, *et al*., "A 3-D-printed lens antenna with tunable varifocal based on the Moire effect," *IEEE Antennas Wirel. Propag. Lett.*, vol. 23, no. 8, pp. 2301–2305, Aug. 2024.

[14]. Y. Cai, P. Mei, X. Q. Lin, and S. Zhang, "A generalized method for gain bandwidth enhancement of transmitarray antennas considering oblique incidences," *IEEE Transactions on Circuits and Systems II: Express Briefs*, vol. 71, no. 1, pp. 121–125, Jan. 2024.

[15]. J.-M. Poyanco, F. Pizarro, and E. Rajo-Iglesias, "3D-printing for transformation optics in electromagnetic high-frequency lens applications," *Materials*, vol. 13, no. 12, p. 2700, Jun. 2020.

[16]. J. M. Poyanco, F. Pizarro, and E. Rajo-Iglesias, "Wideband hyperbolic flat lens in the Ka-band based on 3D-printing and transformation optics," *Appl. Phys. Lett.*, vol. 118, no. 12, Mar. 2021.

[17]. H. Yi, *et al*., "3-D printed millimeter-wave and terahertz lenses with fixed and frequency scanned beam," *IEEE Trans. Antennas Propag.*, vol. 64, no. 2, pp. 442–449, Feb. 2016.

[18]. K. Wang, W. Teng, Z. Chen, H. Wong, and Q. Zhang, "Design of an ultrabroadband circularly polarized 3-D-Printed millimeter-wave lens antenna," *IEEE Trans. Antennas Propag.*, vol. 72, no. 12, pp. 8980 - 8990, Dec. 2024.

[19]. H. Fernandez Alvarez, D. Cadman, A. Goulas, M. Cos Gomez, D. Engstrøm, J. Vardaxoglou, and S. Zhang, "3D conformal bandpass millimeter-wave frequency selective surface with improved fields of view, " *Sci Rep*, 11, 12846, 2021.

[20]. M. Bertrand, *et al*., "Risley Scanner Using a Metasurface Source and a Single Deflector for SATCOM Applications," *IEEE Trans. Antennas Propag*., vol. 72, no. 6, pp. 4839-4851, June 2024.

[21]. X. Liu, *et al*., "Ultrabroadband all-dielectric transmitarray designing based on genetic algorithm optimization and 3-D print technology," *IEEE Trans. Antennas Propag.*, vol. 69, no. 4, pp. 2003–2012, Apr. 2021.

[22]. D. J. Bergman, "The dielectric constant of a composite material—A problem in classical physics," *Phys. Rep.*, vol. 43, no. 9, pp. 377–407, Jul. 1978.

[23]. C. A. Balanis, Advanced Engineering Electromagnetics, John Wiley & Sons, 2012.

[24]. "PREPERM ABS1500, supplied by Avient Corporation," [Online]. Available:https://www.ulprospector.com/plastics/en/datasheet/427049/preperm-abs1500--tp21559.

[25]. "DAK-TL2 SPEAG, Schmid & Partner Engineering AG," [Online]. Available: https://speag.swiss/products/dak/dak-tl-2/.

[26]. M. G. Silveirinha, C. A. Fernandes, and J. R. Costa, "A graphical aid for the complex permittivity measurement at microwave and millimeter wavelengths," *IEEE Microw. Wireless Compon. Lett.*, vol. 24, no. 6, pp. 421–423, Jun. 2014.

[27]. E. B. Lima, S. A. Matos, J. R. Costa, C. A. Fernandes, and N. J. G. Fonseca, "Circular polarization wide-angle beam steering at Ka-band by In-Plane translation of a plate lens antenna," *IEEE Trans. Antennas Propag.*, vol. 63, no. 12, pp. 5443–5455, Dec. 2015.

[28]. H. Yang, *et al*., "A study of phase quantization effects for reconfigurable reflectarray antennas," *IEEE Antennas Wirel. Propag. Lett.*, vol. 16, pp. 302–305, 2017.

[29]. A.-E. Mahmoud, W. Hong, Y. Zhang, and A. Kishk, "W-band mutlilayer perforated dielectric substrate lens," *IEEE Antennas Wirel. Propag. Lett.*, vol. 13, pp. 734–737, 2014.